PLASMA DYNAMICS

IV. PLASMAS AND CONTROLLED NUCLEAR FUSION

A. Waves and Radiation

Academic and Research Staff

Prof. G. Bekefi   Prof. S. C. Brown   Prof. R. J. Taylor
Prof. W. P. Allis   Prof. B. Coppi   J. J. McCarthy
Prof. A. Bers   Prof. E. V. George   W. J. Mulligan
                         Prof. P. A. Politzer

Graduate Students

F. W. Chambers   D. O. Overskei
R. J. Hawryluk   M. L. Vianna

1. COMPARISON OF STARK-BROADENED OPTICAL LINE SHAPES CAUSED BY HOLTSMARK AND GAUSSIAN MICROFIELDS

G. Bekefi, C. Deutsch, C. Coulaud, M. Sassi

[Dr. Deutsch, Dr. Coulaud and Dr. Sassi are at the Université de Paris where part of this work was carried out.]

It is well known that the fluctuating microfield of a plasma in thermodynamic equilibrium having many particles in a Debye sphere is well represented by the Holtsmark-Hooper probability distribution[1] W(E). On the other hand, a thermal plasma having very few particles in the Debye sphere, or a highly turbulent nonthermal plasma, are expected to have a probability distribution approaching a Gaussian.[2,3] As we pointed out in our last report,[4] a Stark-broadened optical line shape caused by a Gaussian distribution can differ significantly from the line shape resulting from the Holtsmark-Hooper distribution. Such differences could be exploited in determining the fluctuating electric field in nonclassical plasmas.

In this report we compare the Gaussian and Holtsmark-Hooper induced profiles for the He I $2\,^3P$-$4\,^3D$ allowed line at 4471 Å and the neighboring $2\,^3P$-$4\,^3F$ forbidden line at 4470 Å. The effect of electron impacts is omitted throughout these computations. Figure IV-1a illustrates the line profiles for a Gaussian electric field of the form[4]

$$W(E)\,dE = 4\pi \left[\frac{1}{2\pi\sigma}\right]^{3/2} E^2\, e^{-E^2/2\sigma}\, dE, \tag{1}$$

where σ is the standard deviation. The curves shown in Fig. IV-1a refer to three different values of the rms electric field
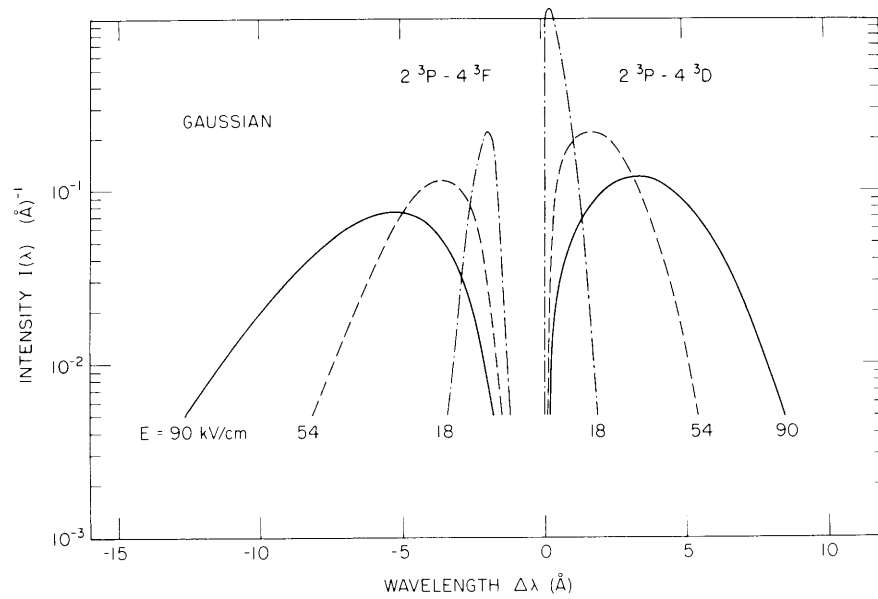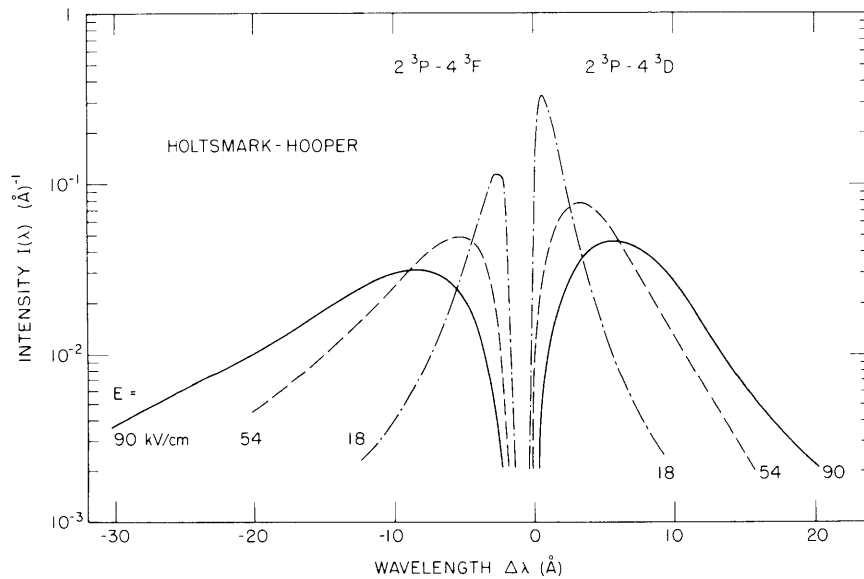
Fig. IV-1. Line profiles of the He I $2\,^3P\,{-}4\,^3D$ allowed line at 4471 Å and of the $2\,^3P\,{-}4\,^3F$ forbidden line at 4470 Å. The wavelength $\Delta\lambda = 0$ on the abscissa corresponds to the wavelength position of the unperturbed allowed line. The total area under the combined allowed and forbidden lines is normalized in each case so that $\int_0^\infty I(\lambda)\,d\lambda = 1$.

(a) Three different values of the Gaussian-distributed electric microfield.
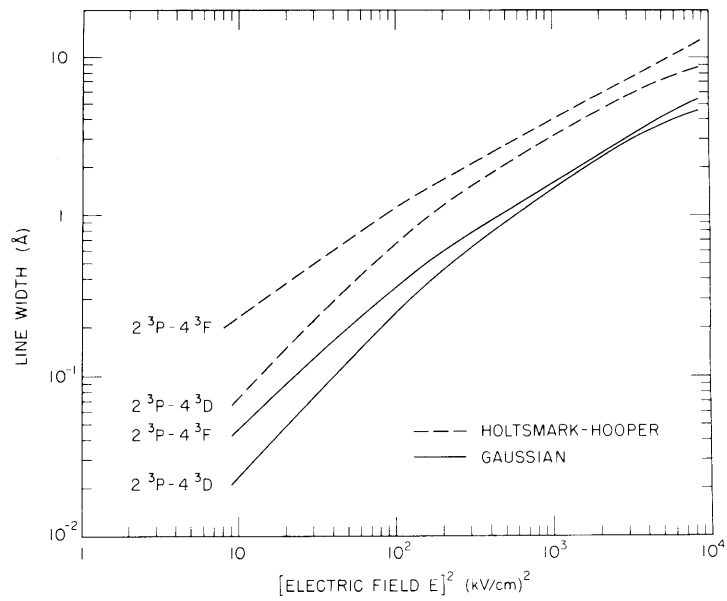(b) Corresponding computations for the Holtsmark-Hooper distribution.

Fig. IV-2. Full linewidth measured at half the peak intensity for the allowed and forbidden lines as a function of the strength of the fluctuating electric field squared.
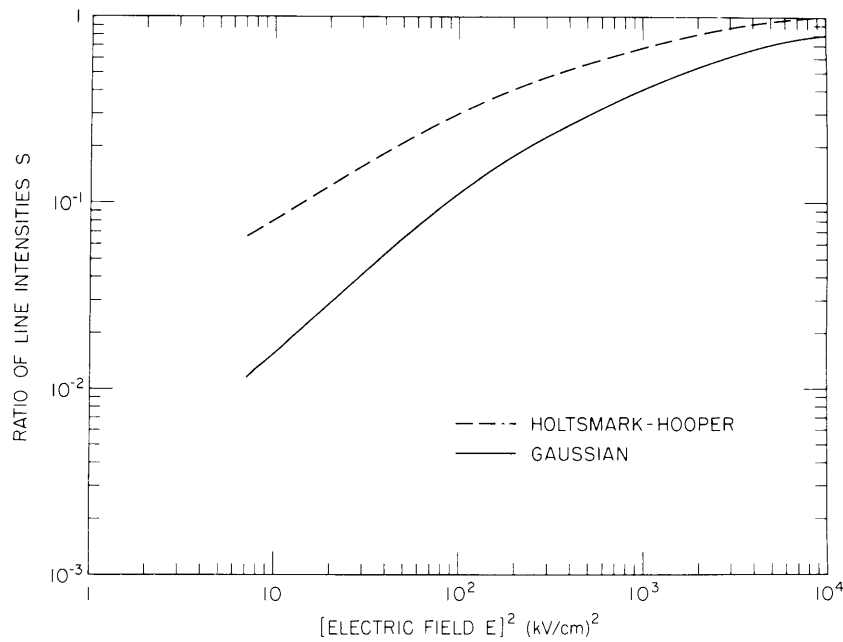

Fig. IV-3. Ratio S of the integrated forbidden line intensity to the integrated allowed line intensity as a function of the fluctuating electric field squared.

$$\sqrt{\langle E^2 \rangle} = \left[\int_0^\infty E^2 W(E)\, dE \right]^{1/2} = \sqrt{3\sigma}. \tag{2}$$

Figure IV-1b shows corresponding computations for the Holtsmark-Hooper distribution (note that the identical Fig. IV-3 in our last report[4] was captioned erroneously as Gaussian, rather than Holtsmark-Hooper). The electric field values quoted in Fig. IV-1b refer to the Holtsmark "normal" field; the rms electric field for this distribution is infinite and thus is physically not meaningful. Comparing both parts of Fig. IV-1, we see immediately that the Gaussian profiles (a) are much narrower and that the wings of the lines fall off much more sharply than those for the Holtsmark-Hooper distribution (b). The differences in the wings reflect the fact that for large electric fields W(E) of the Gaussian distribution falls off exponentially, while W(E) of the Holtsmark-Hooper distribution falls off more slowly (as $E^{-5/2}$).

In Fig. IV-2 we show the widths of the allowed and forbidden lines for the two different distributions W(E) and in Fig. IV-3 we show the ratio of integrated line intensities. Calculations similar to those described above are now being carried out for the case of the "one-dimensional" Gaussian distribution

$$W(E)\, dE = \frac{1}{\sqrt{2\pi\sigma}}\, e^{-E^2/2\sigma}\, dE$$

$$\int_{-\infty}^\infty W(E)\, dE = 1$$

$$\sqrt{\langle E^2 \rangle} = \left[\int_{-\infty}^\infty E^2 W(E)\, dE \right]^{1/2} = \sqrt{\sigma}.$$

Such a distribution is relevant for many plasmas in which the turbulence is induced by waves propagating primarily along one direction.

References

1. C. F. Hooper, Phys. Rev. 165, 215 (1968).
2. V. I. Kogan, V. S. Lisitza, and A. D. Selidovkin, Paper 4.1.2.2, 8th International Conference on Phenomena in Ionized Gases, Vienna, 1967 (Springer Verlag, Berlin, 1968), p. 273.
3. M. Raether and M. Yamada, Phys. Letters 44A, 241 (1973).
4. G. Bekefi and C. Deutsch, Quarterly Progress Report No. 110, Research Laboratory of Electronics, M.I.T., July 15, 1973, p. 55.

2. PULSE EVOLUTION OF SECOND-ORDER WAVE-WAVE
   INTERACTIONS

A. Bers, F. W. Chambers, R. J. Hawryluk

Nonlinear plasma instabilities are expected to play an important role in laser-pellet fusion experiments.[1] The detailed time-space evolution of such instabilities may be significant in assessing their importance. Knowledge of the pulse evolution is also required for properly designing small-scale experiments for observing such instabilities. In this report we summarize the main features of the one-dimensional evolution of second-order (parametric) plasma instabilities, and give illustrative calculations. The detailed theoretical development and major results have been reported elsewhere.[2,3]

Consider the nonlinear coupling of two waves caused by the presence of a pump wave. Let the pump wave be characterized by a fixed (normalized) amplitude a_{10}, frequency ω_1, and wave number k_1, and let the waves that couple be characterized, respectively, by a_2, ω_2, k_2, and a_3, ω_3, k_3. Also, let γ_2 and $-c$, respectively, be the weak damping rate and group velocity of wave 2, and γ_3 and v be the similar quantities for wave 3. The nonlinear coupling of these waves to second-order will induce a slow time-and-space variation of their amplitudes given[2] by

$$\left(\frac{\partial}{\partial t} - c\,\frac{\partial}{\partial z} + \gamma_2\right) a_2(z,t) = -p_2 K^* a_{10} a_3^*(z,t) \tag{1}$$

$$\left(\frac{\partial}{\partial t} + v\,\frac{\partial}{\partial z} + \gamma_3\right) a_3(z,t) = -p_3 K^* a_{10} a_2^*(z,t), \tag{2}$$

where $p = \pm 1$ is the energy sign (parity) of the unperturbed waves, and the coupling coefficient K has been given elsewhere by Bers.[2] (Computations of K for some specific interactions were given in a previous report.[4])

The Green's function solution of these equations is given by

$$G(z,t) = \int_L \frac{ds}{2\pi} e^{-ist} \int_F \frac{d\kappa}{2\pi} e^{i\kappa z} \frac{1}{D(\kappa,s)}, \tag{3}$$

where

$$D(\kappa,s) = (s + c\kappa + i\gamma_2)(s - v\kappa + i\gamma_3) + \gamma^2 \tag{4}$$

is the dispersion relation, and

$$\gamma^2 = p_1 p_2 |K|^2 |a_{10}|^2 \tag{5}$$

is the maximum possible growth (for $p_1 p_2 > 0$) rate of the interaction, which occurs when the uncoupled waves are undamped, that is, $\gamma_2 = 0$ and $\gamma_3 = 0$. This can be established directly from $D(\kappa, s) = 0$ by solving for the maximum s_i as a function of $\kappa = \kappa_r$, where subscripts i and r designate the imaginary and real parts. Furthermore, in the undamped case the instability is absolute when the group velocities of the two unperturbed waves are opposite to each other, as we chose them to be in Eqs. 1 and 2. The growth rate of this absolute instability can be found from the simultaneous solution of $D(\kappa, s) = 0$ and $(\partial D/\partial \kappa) = 0$. It is found to be

$$s_{oi} = \frac{2(cv)^{1/2}}{(c+v)} \gamma. \tag{6}$$

Similarly, when the damping of the waves is finite we can establish the threshold for instability as

$$\gamma^2 > \gamma_2 \gamma_3 \overset{\Delta}{=} \gamma_c^2 \tag{7}$$

and the threshold for absolute instability as

$$\gamma^2 > \frac{(\gamma_2 v + \gamma_3 c)^2}{4cv} = \frac{cv}{4}(a_2 + a_3)^2 \overset{\Delta}{=} \gamma_a^2, \tag{8}$$

where $a_{2,3}$ are the spatial damping rates of the uncoupled waves. For $\gamma_c < \gamma < \gamma_a$ the instability is convective.

A more complete picture of the instability can be obtained from a study of the asymptotic pulse shape. This is determined by examining the absolute instability growth rate as a function of an observer's frame velocity V. We thus transform Eq. 4 to $D(\kappa, s + \kappa V) \overset{\Delta}{=} D_V$ and solve for the roots of $D_V = 0$ and $\partial D_V / \partial \kappa = 0$. This gives

$$s_{oi}(V) = \frac{2\gamma}{(c+v)} [(V+c)(v-V)]^{1/2} - \frac{\gamma_2(v-V) + \gamma_3(V+c)}{c+v}, \tag{9}$$

which for $V = 0$ and $\gamma_2 = \gamma_3 = 0$ reduces to Eq. 6. A plot of s_{oi} as a function of V gives the asymptotic pulse-shape evolution, since $s_{oi} t \sim \ln |G(z, t \to \infty)|$ and $Vt = z$. The three curves in Fig. IV-4 show this pulse shape at the threshold for instability ($\gamma = \gamma_c$), when it is convectively unstable ($\gamma_c < \gamma < \gamma_a$), and at the threshold for absolute instability ($\gamma = \gamma_a$). All of the important characteristics of the pulse shape can be determined analytically. First, we note that

$$s_{oi}(-c) = -\gamma_2 \tag{10}$$

$$s_{oi}(v) = -\gamma_3. \tag{11}$$

Thus wave damping has the effect of narrowing the growing ($s_{oi} > 0$) part of the pulse,

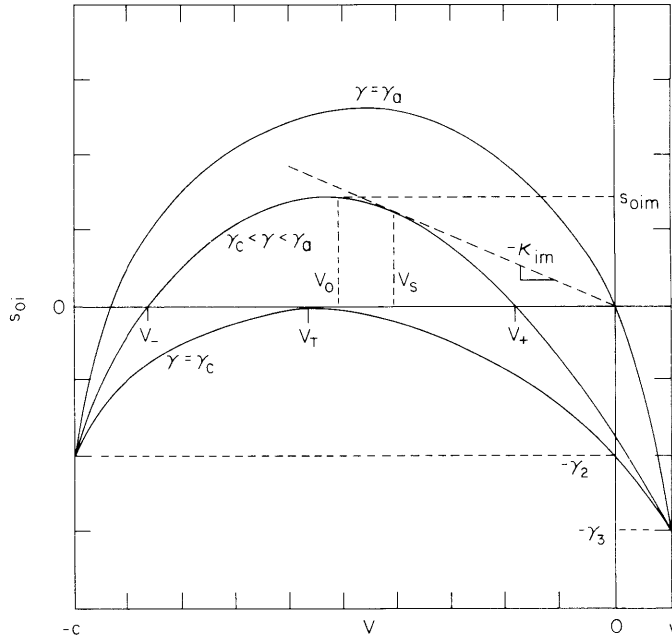Fig. IV-4. Sketch of s_{oi} vs V for various coupling strengths, as given by γ, and with the wave-damping rates γ_2 and γ_3 kept fixed.

and thus reduces its expansion rate. The pulse-edge velocities $V = V_\pm$ can be found by setting Eq. 9 to zero. This gives

$$V_\pm = \frac{V_T - \left(\frac{c-v}{2}\right)\Gamma^2 \pm \left(\frac{c+v}{2}\right)\frac{2\gamma\Gamma}{\gamma_2+\gamma_3}}{1 + \Gamma^2}, \tag{12}$$

where

$$\Gamma^2 = \frac{4\left(\gamma^2-\gamma_c^2\right)}{(\gamma_2+\gamma_3)^2} \tag{13}$$

and

$$V_T = \frac{\gamma_2 v - \gamma_3 c}{\gamma_2 + \gamma_3} = (\text{sgn } V_T)(vc)^{1/2} \frac{\left(\gamma_a^2 - \gamma_c^2\right)^{1/2}}{(\gamma_2 + \gamma_3)/2} \tag{14}$$

is clearly the pulse velocity at the threshold for instability ($\gamma = \gamma_c$ and hence $\Gamma^2 = 0$). At the absolute instability threshold ($\gamma = \gamma_a$, see Eq. 8) we find from Eq. 12 that $V_{\text{sgn } V_T} = 0$, as expected, and above this threshold we approach the case of coupling of undamped waves for which $V_+ = v$ and $V_- = -c$. The maximum of the asymptotic pulse (s_{oim}) and the velocity with which it moves (V_0) can be found by maximizing Eq. 9 with respect to V. The results can be written

$$V_0 = -\left(\frac{c-v}{2}\right)\left\{1 - \left(\frac{c+v}{c-v}\right)\left(\frac{\gamma_2 - \gamma_3}{2\gamma}\right)\left[1 + \left(\frac{\gamma_2 - \gamma_3}{2\gamma}\right)^2\right]^{-1/2}\right\}$$

$$= \frac{V_T + \left(\frac{c-v}{2}\right)\left[1 - (1+\Gamma^2)^{1/2}\right]}{(1+\Gamma^2)^{1/2}}, \tag{15}$$

and

$$s_{\text{oim}} = \gamma\left\{\left[1 + \left(\frac{\gamma_2 - \gamma_3}{2\gamma}\right)^2\right]^{1/2} - \left(\frac{\gamma_2 + \gamma_3}{2\gamma}\right)\right\}$$

$$= \gamma\left(\frac{\gamma_2 + \gamma_3}{2\gamma}\right)\left\{(1+\Gamma^2)^{1/2} - 1\right\}. \tag{16}$$

At the threshold for instability ($\gamma = \gamma_c$ and hence $\Gamma^2 = 0$) $s_{\text{oim}} = 0$ and $V_0 = V_T$, as would be expected. Far above this threshold $V_0 \to -(c-v)/2$ and $s_{\text{oim}} \to \gamma$, which is the maximum possible growth rate. We note that s_{oim} is independent of the group velocities of the unperturbed waves. Finally, when the pulse is convectively unstable ($\gamma_c < \gamma < \gamma_a$) it is of interest to determine the maximum spatial growth rate (κ_{im}). This can be determined either from Eq. 9, together with the construction shown in Fig. IV-4, or directly from the dispersion relation (Eq. 4) for real s, by noting that $\kappa_{\text{im}} = \kappa_i$ ($s = s_{\text{rm}}$), where s_{rm} is determined from $\partial\kappa_i/\partial s_r = 0$; V_s is then given by $(\partial\kappa_r/\partial s_r)_{s_{\text{rm}}}^{-1}$. The results are

$$V_s = \frac{2cv}{(c+v)} \frac{\left(\gamma_a^2 - \gamma^2\right)^{1/2}}{(\text{sgn } V_T)\,\gamma_a + \left(\frac{c-v}{c+v}\right)\left(\gamma_a^2 - \gamma^2\right)^{1/2}} \tag{17}$$
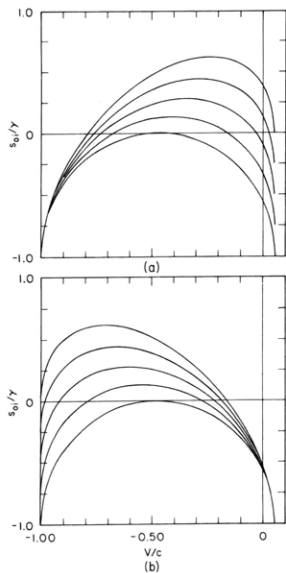
Fig. IV-5.

Computed plots of s_{oi} vs V; s_{oi} normalized to γ, V normalized to c, v/c chosen as .05.

(a) $s_{oi}(V)$ vs mode 3 damping, with mode 2 damping fixed. $\gamma_2/\gamma = 1$; $\gamma_3/\gamma = 0$, .25, .50, .75, 1.0.

(b) $s_{oi}(V)$ vs mode 2 damping, with mode 3 damping fixed. $\gamma_3/\gamma = 1$; $\gamma_2/\gamma = 0$, .25, .50, .75, 1.0.
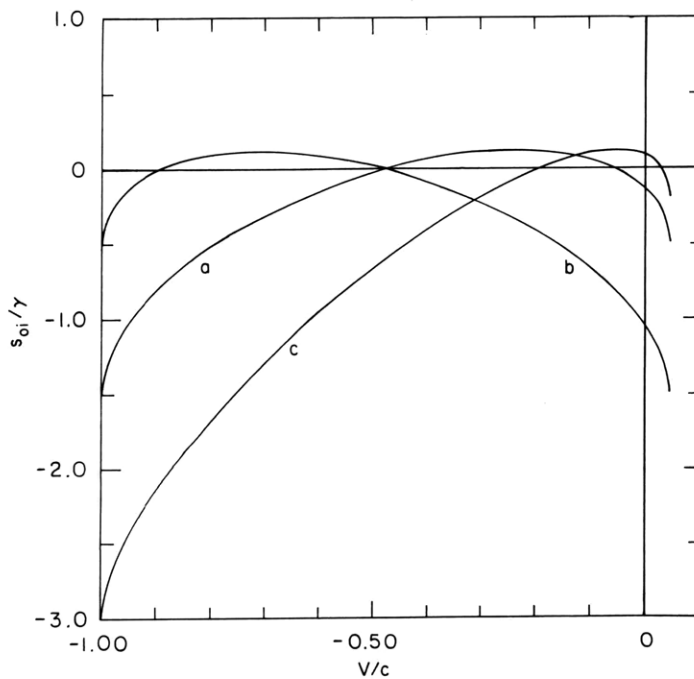

Fig. IV-6. $s_{oi}(V)$ plots for the pulses illustrated in Fig. IV-7. v/c = .05, (a) $\gamma_2/\gamma = 1.5$, $\gamma_3/\gamma = .5$; (b) $\gamma_2/\gamma = .5$, $\gamma_3/\gamma = 1.5$; (c) $\gamma_2/\gamma = 3.0$, $\gamma_3/\gamma = .2$.

and

$$\kappa_{im} = -(\text{sgn } V_T) \left[\left(\frac{\gamma_a^2 - \gamma_c^2}{cv} \right)^{1/2} - \left(\frac{\gamma_a^2 - \gamma^2}{cv} \right)^{1/2} \right].$$ (18)

For $\gamma_a^2 \gg \gamma_c^2$ this growth rate is largest near the absolute instability threshold ($\gamma \sim \gamma_a$), where it is approximately $\gamma_a/(cv)^{1/2}$, and decreases from this value by a factor $\left(\gamma^2 - \gamma_c^2 \right)/2\gamma_a^2$ when $\gamma \ll \gamma_a$.

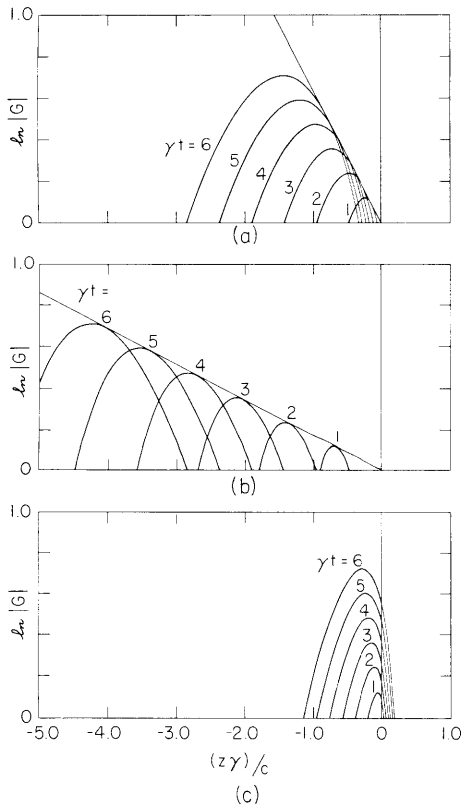Figures IV-5, IV-6, and IV-7 give numerically calculated asymptotic pulse shapes

Fig. IV-7.

Computed plots of the spatial development of the time asymptotic exponential envelope of the Green's function $v/c = .05$.

(a) Slow convective pulse $\gamma_2/\gamma = 1.5$, $\gamma_3/\gamma = .5$.

(b) Fast convective pulse $\gamma_2/\gamma = .5$, $\gamma_3/\gamma = 1.5$.

(c) Absolutely unstable pulse $\gamma_2/\gamma = 3.0$, $\gamma_3/\gamma = .2$.

for various conditions of wave damping. The ratio v/c was kept fixed at a small value, which is typical of interactions of stimulated Brillouin or Raman scattering. Figure IV-5 shows the effect of varying the damping rate of one or the other wave. We note in particular (Fig. IV-5b) that when the backscattered wave is weakly damped the main portion of the unstable pulse moves very rapidly; only large increases in damping that almost quench the instability can reduce this motion. Figures IV-6 and IV-7 illustrate the time-space evolution of convective and absolute instabilities. Note in particular (Fig. IV-7a and b) that convective instabilities may be very different in nature, depending on their pulse-edge velocities. This has important consequences with respect to the evolution of such instabilities in an interaction region of finite extent.

References

1. J. Nuckolls, J. Emmett, and L. Wood, Phys. Today 26, 46 (1973).

2. A. Bers, Notes on Lectures: Linear Waves and Instabilities, given at Ecole d'Eté de Physique Théorique, Les Houches, France, July 1972 (Gordon and Breach, New York, in press).

3. A. Bers, "Theory of Absolute and Convective Instabilities," in Proc. Invited Papers: International Congress on Waves and Instabilities in Plasma, April 1-7, 1973, Institute for Theoretical Physics, University of Innsbruck, Innsbruck, Austria (in press).

4. F. W. Chambers, R. J. Hawryluk, and A. Bers, Quarterly Progress Report No. 110, Research Laboratory of Electronics, M.I.T., July 15, 1973, pp. 45-55.

IV. PLASMAS AND CONTROLLED NUCLEAR FUSION

B. Diffusion and Turbulence

Academic Research Staff

Prof. T. H. Dupree
Prof. L. M. Lidsky
Prof. P. A. Politzer

Graduate Students

A. R. Forbes
A. Hershcovitch

J. C. Hsia
P. M. Margosian

1. SOME FAST INEXPENSIVE LINE PULSERS NOW IN USE

U. S. Atomic Energy Commission (Contract AT(11-1)-3070)

A. Hershcovitch, P. M. Margosian

For a great variety of physics experiments, a fast (a few nanoseconds rise and fall), high-voltage (a few kilovolts) pulse generator is frequently needed. This is not a new problem. A standard solution[1] is to charge a delay line, then switch it into its characteristic impedance (Fig. IV-8) to give $V_{pulse} = \frac{1}{2} V_{charge}$. A variation of this is the Blumlein pulser (Fig. IV-9) which uses two identical delay lines and gives $V_{pulse} = -V_{charge}$, thereby providing a higher voltage pulse for a given switch. In both cases the rise time of the pulse is determined by the turn-on time of the switch; the fall time is ideally a reflection of the rise, but in practice is limited by high-frequency properties of the delay line. This report describes a collection of inexpensive line pulsers that we are using.
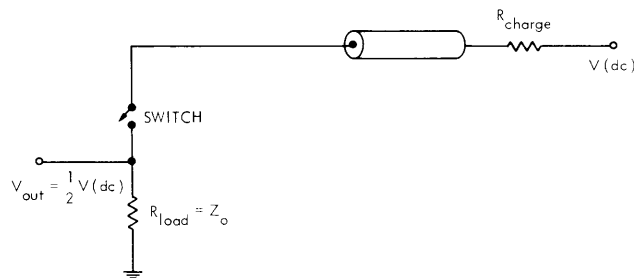

Fig. IV-8.   Standard line pulser.

The traditional switches — rotating mechanical, rotating spark gap, and thyratron — are discussed by Glascoe and Lebacqz.[1] A rotating mechanical switch, with 4 electrical
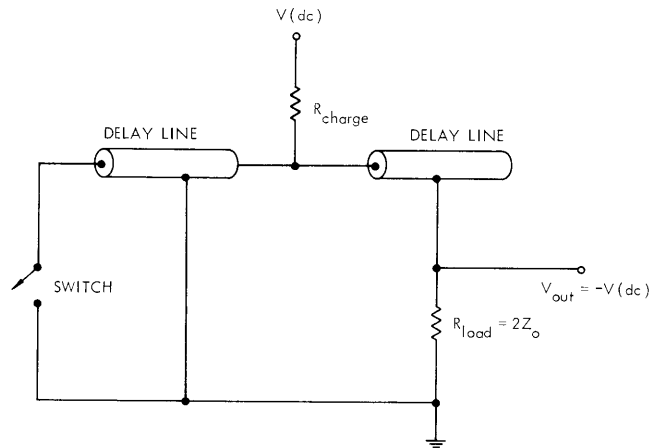
Fig. IV-9. Blumlein pulser.

contacts embedded in a bakelite wheel, a sliding contact wiper, and a motor was built by Kenneth Rettman in our laboratory. This switch, using the circuit of Fig. IV-8 with RG58 A/U cable as delay line, exhibits rise times of 3-5 ns for V_{charge} = 300 to 3000 V. We have built thyratron pulsers using an EG&G krytron (current limited to approximately 10 A) and using a coaxial hydrogen thyratron; in both cases rise times were near 10 ns. These traditional switches tend to be costly (approximately \$200 for a fast thyratron and approximately 5 days labor to build a rotating switch). The krytron has a limited life. These switches also exhibit a good deal of jitter.
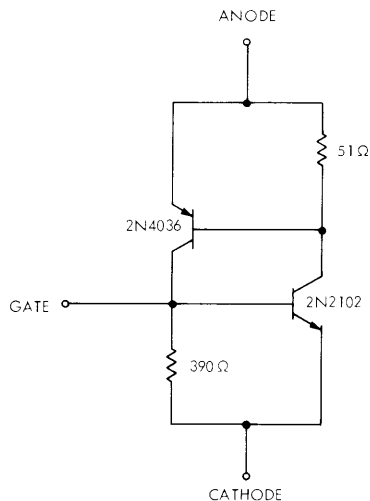

Fig. IV-10. Homemade fast SCR.

An alternative to these is the semiconductor controlled rectifier (SCR). A fast SCR was built from 2 transistors (Fig. IV-10); it provides a rise time of 20 ns current up

to 3-4 A, handles up to 150 V, and costs approximately $3 for parts. A stack of 16 of these SCRs is regularly used in the circuit shown in Fig. IV-8 with an artificial line for 150-1500 V. A fast commercial unit is available from Unitrode Corporation (GB-301) for ~$9 (30 A, 20 ns, 100 V). A Blumlein pulser (Fig. IV-9) was built with 10 of these with two RG58 A/U cables to provide 50-1000 V pulses with rise time of 20 ns and length of 400 ns. For both types of SCR, there was no loss of speed from stacking, as
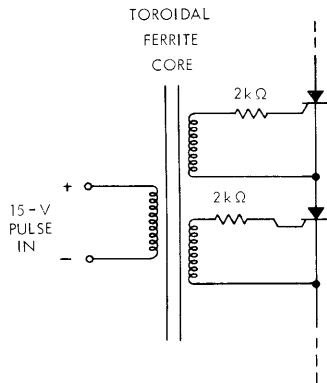
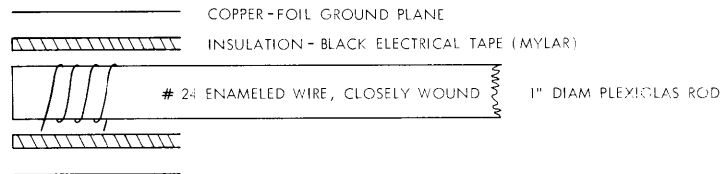Fig. IV-11.   Triggering for stacked SCRs.

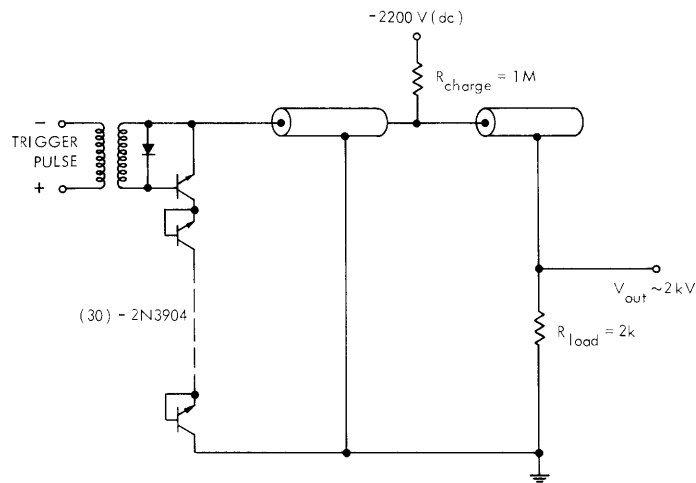Fig. IV-12.   High-impedance delay line (~1000 Ω).

Fig. IV-13.   Avalanche pulser.

long as all were triggered simultaneously through a transformer (Fig. IV-11).

Another alternative is to use the avalanche transistor.[3] This has a current limitation (1-2 A) and produces a nearly fixed voltage (close to V_{ceo} of the transistor), but very high speed (less than 1 ns is possible). For a high-voltage pulse it is necessary to stack many transistors (e. g., 2N3904) and build a high-impedance delay line (~1000 Ω). Two 1000 Ω lines were built (Fig. IV-12) using a technique suggested by Lidsky and Rose.[2] A Blumlein pulser was built that used 30 of the 2N3904 transistors and two 1000 Ω lines (Fig. IV-13); it provided ~2 kV into 2000 Ω with 10 ns rise time and cost less than $10 for parts. In building this type of pulser it is necessary to exercise some care in the choice of the charging resistor and the number of stacked transistors in order to prevent oscillation and misfiring; the bias current through the transistors should be ~20 μA when the lines are charged to operating voltage.

Of the switching techniques discussed, the fast commercial SCRs are the most flexible, and the avalanche circuit is the fastest and least expensive.

We have received helpful suggestions from Donald L. Cook, Donald P. Hutchinson, Professor Lawrence M. Lidsky, and Professor Peter A. Politzer.

References

1. G. N. Glasoe and J. V. Lebacqz, Pulse Generators (Dover Publications, Inc., New York, 1948).

2. L. M. Lidsky and D. J. Rose, Rev. Sci. Instr. 34, 1223-1227 (1963).

3. B. H. Bell, Electronic Design, Vol. 12, June 8, 1964.

2. LINEAR ANALYSIS OF THE "ONE-HALF CYCLOTRON FREQUENCY" INSTABILITY

A. Hershcovitch, P. A. Politzer

Introduction

It has been observed[1-4] that the one-half cyclotron frequency instability occurs in counterstreaming finite cross-section beams in a magnetic field. The instability is caused by coupling between a space-charge wave on one beam and a backward cyclotron wave on the other.[3,4] This instability occurs only when the beams have a finite cross section such that the variation in local charge density caused by the longitudinal wave affects the cyclotron wave on the oppositely directed beam (i. e., backward cyclotron wave).

Linear analysis of this instability[1-4] shows good agreement between the linear

theory and the experimental results[3] with regard to the threshold density for the onset of the instability. There is no agreement, however, concerning the prediction of the thermal spread of the beams which is needed to "saturate" this instability.

Previous linear theories related to cold beams. This is rather unrealistic, since the beams have a finite temperature that is equal to the cathode temperature. Murakami and Lidsky[3] have observed that the beam temperature increases as the instability grows, and that after 1 μs the instability that occurs at a frequency $\Omega/2$ seems to saturate.

Therefore it is logical to make the analysis by considering finite temperature beams. Quasi-linear theory will not be used now. It is assumed that the beams evolve to some thermal spread close to that needed to stabilize the instability. At this point, the linear theory is applied. First, a dispersion relation for finite temperature beams, which at the limit of zero temperature reduces to the old dispersion relation, will be derived. Next, this dispersion relation will be used to analyze Murakami's experiment,[3,4] and to calculate the thermal spread needed for stabilization. It <u>will</u> <u>be</u> <u>shown</u> <u>that</u> <u>the</u> <u>insta-</u> <u>bility</u> <u>does</u> <u>not</u> <u>saturate;</u> <u>only</u> <u>its</u> <u>frequency</u> <u>changes.</u>

Dispersion Relation for Two Hot Counterstreaming Electron Beams for an Infinite Homogeneous Medium in a Uniform Magnetic Field

The dispersion relation is derived by using the Harris dispersion relation,[5] and by considering two drifting Maxwellians.

The Harris dispersion relation is

$$\epsilon(\underline{k}, \omega) = 0 = 1 - \sum_j \frac{\omega_{pj}^2}{k^2} \int d^3\underline{v} \sum_{n=-\infty}^{\infty} \frac{J_n^2\left(\frac{k_\perp v_\perp}{\Omega_j}\right)}{k_z v_z - n\Omega_j - \omega} \left[k_z \frac{\partial f_{oj}}{\partial v_z} + \frac{n\Omega_j}{v_\perp} \frac{\partial f_{oj}}{\partial v_\perp} \right]. \tag{1}$$

The distribution function that is assumed is

$$f_o = \frac{1}{\pi^{3/2} v_T^3} \exp\left\{ -\frac{v_\perp^2}{v_T^2} \right\} \left[\exp\left\{ -\frac{(v_z - v_o)^2}{v_T^2} \right\} + \exp\left\{ -\frac{(v_z + v_o)^2}{v_T^2} \right\} \right],$$

where $v_o \gg v_T$, $v_{T\perp} = v_{Tz} = v_T$, with v_o the streaming velocity, and v_T the thermal spread. In this case, there are only electrons, therefore $\omega_{pj} = \omega_{pe} = \omega_p$ and $\Omega_j = -\Omega_e = -\Omega$. With this distribution function, the Harris dispersion relation in cylindrical coordinates becomes

$$0 = 1 + \frac{\omega_p^2}{k^2} \frac{4}{\sqrt{\pi}} \frac{1}{v_T^5} \sum_{n=-\infty}^{\infty} \int_0^{\infty} v_\perp \, dv_\perp \exp\left\{-\frac{v_\perp^2}{v_T^2}\right\} J_n^2\left(\frac{k_\perp v_\perp}{-\Omega}\right) \int_{-\infty}^{\infty} dv_z$$

$$\times \left[\frac{k_z(v_z-v_o) - n\Omega}{k_z v_z - n\Omega - \omega} \exp\left\{-\frac{(v_z-v_o)^2}{v_T^2}\right\} + \frac{k_z(v_z+v_o) - n\Omega}{k_z v_z - n\Omega - \omega} \exp\left\{-\frac{(v_z+v_o)^2}{v_T^2}\right\}\right].$$

(2)

Now, in Eq. 2, the integrations over v_z and $v_\perp$ can be done separately. For the integration over $v_\perp$, Weber's second exponential integral[6] is used. The integration over v_z is performed by using the plasma dispersion function[7] and its derivatives. After some manipulations, the following dispersion relation is obtained.[8]

$$\epsilon(\underline{k}, \omega) = 0 = 1 - \frac{\omega_p^2}{k^2} \frac{2}{v_T^3} \exp\left\{-\frac{k_\perp^2 v_T^2}{2\Omega^2}\right\} \sum_n I_n\left(\frac{k_\perp^2 v_T^2}{2\Omega^2}\right)\left[-2v_T + \left(\frac{-\omega + k_z v_o}{k_z}\right)\right.$$

$$\times Z\left(\frac{\omega - k_z v_o + n\Omega}{k_z v_T}\right) + \left(\frac{-\omega - k_z v_o}{k_z}\right) Z\left(\frac{\omega + k_z v_o + n\Omega}{k_z v_T}\right)\right].$$

(3)

In the limit of zero v_T, by using the properties of the z function[7] and Bessel functions,[6,9] Eq. 3 reduces[8] to

$$\epsilon(\underline{k}, \omega) = 1 - \frac{\omega_p^2}{(\omega-k_z v_o)^2} - \frac{\omega_p^2}{(\omega+k_z v_o)^2} + \frac{2\omega_p^2}{\Omega^2 - (\omega-k_z v_o)^2} + \frac{2\omega_p^2}{\Omega^2 - (\omega+k_z v_o)^2}.$$

(4)

This is in agreement with Maxum and Trivelpiece.[1]

Analysis of Murakami's Experiment Using the Dispersion Relation (Eq. 3)

Stability analysis of Eq. 3 is now performed by using the parameters of Murakami's experiment.[3,4] These parameters are beam radius 1 mm = r_b; $\Omega = 2.8 \times 10^8$ Hz = $2\pi \times 2.8 \times 10^8$ rad/s; $\omega_p = 0.1\,\Omega$; $E_o = 1$ keV, therefore $v_o^2 = 35.5 \times 10^{17}$ cm^2/s^2.

Recall that the dispersion relation (Eq. 3) is valid for an infinite homogeneous electron gas in a constant uniform magnetic field. In Murikami's experiment the beams are narrow, with constant density across the cross section. Thus, in order to simulate the geometrical effects, the value of the perpendicular component of the wavelength is assumed to be equal to the beam radius. Hence an infinite homogeneous medium is assumed with $k_\perp = \frac{2\pi}{r_b}$. This assumption and the assumed distribution function are

the major assumptions, and they seem to be very realistic.

By using the parameters of this experiment, Eq. 3 can be simplified by using the following approximations.

(a) For a strong resonant wave-particle interaction to occur the phase velocity of the unstable waves has to be close to the velocity of some electrons. Therefore $\frac{\omega - k_z v_o}{k_z v_T} \lesssim 1$ for strong wave-particle resonant interaction to occur. Since for large arguments the Z function is small,[7] the main contribution from the first Z function in Eq. 3 is for n = 0, and the main contribution from the second Z function in Eq. 3 is for n = -1. This is indeed consistent with the physical model[3,4] which attributes the instability to the coupling between the space-charge wave (n = 0) and the backward cyclotron wave (n = -1). Therefore, the summation in Eq. 3 needs to be done only for n = 0 and n = -1.

(b) For an observed initial thermal spread[3,4] of 20 eV we obtain $\frac{k_\perp^2 v_T^2}{2\Omega^2} \sim 10$. Therefore, since $I_n(x) \rightarrow \frac{e^x}{\sqrt{2\pi x}}$ for $x \gg n$, $I_n\left(\frac{k_\perp^2 v_T^2}{2\Omega^2}\right)$ in Eq. 3 can be taken outside the summation sign.

With these approximations, Eq. 3 becomes

$$0 = 1 - \frac{\omega_p^2}{k^2} \frac{2}{v_T^3} \frac{1}{\sqrt{2\pi \frac{k_\perp^2 v_T^2}{2\Omega^2}}} \left\{ -4v_T + \left(\frac{-\omega + k_z v_o}{k_z}\right) Z\left(\frac{\omega - k_z v_o}{k_z v_T}\right) \right.$$

$$+ \left(\frac{-\omega - k_z v_o}{k_z}\right) Z\left(\frac{\omega + k_z v_o}{k_z v_T}\right) + \left(\frac{-\omega + k_z v_o}{k_z}\right) Z\left(\frac{\omega - k_z v_o - \Omega}{k_z v_T}\right)$$

$$+ \left(\frac{-\omega - k_z v_o}{k_z}\right) Z\left(\frac{\omega + k_z v_o - \Omega}{k_z v_T}\right) \right\}. \tag{5}$$

The arguments of the first and last Z functions are less than one. The other two have arguments that are much greater than one. Accordingly, the Z functions in Eq. 5 are expanded. In this analysis, the case of marginal stability is considered; that is, Im $\omega \approx 0$. Hence we use the expansions for the Z functions, keeping first terms only. At this point, further approximations can be made. By considering the following arguments, the second and third exponentials can be neglected. The other exponentials have small arguments, hence they can be approximated to one. Thus the dispersion relation reduces to

$$2\omega^2 - \omega\left(\Omega + \frac{i\sqrt{\pi}}{2} k_z v_T\right) - \frac{3k_z^2 v_T^2}{2} + \frac{\sqrt{\pi}\ k^2 k_z^2 k_\perp v_T^5}{4\omega_p^2 \Omega} + 2k_z^2 v_o^2 - k_z v_o \Omega = 0. \tag{6}$$

The solution to Eq. 6 is

$$\omega = \frac{\Omega}{4} + \frac{i\sqrt{\pi}}{8} k_z v_T \pm \frac{1}{4}\left[\Omega^2 + i\sqrt{\pi}\ \Omega k_z v_T - \frac{\pi}{4} k_z^2 v_T^2 \right.$$

$$\left. - 8\left(2k_z^2 v_o^2 - k_z v_o \Omega\right) + \frac{\sqrt{\pi}\ k^2 k_z^2 k_\perp v_T^5}{4\omega_p^2 \Omega} - \frac{3}{2} k_z^2 v_T^2 \right]^{1/2} .$$

Roughly, for $v_T < 2.7 \times 10^8$ cm/s, that is, for thermal energy $E_T < 20$ eV, the roots of ω are $\omega_1 \approx \frac{\Omega}{2} + i(.2 k_z v_T + .7\sqrt{\Omega k_z v_T})$, which is the one-half cyclotron frequency instability, and $\omega_2 \approx 0 + i(.2 k_z v_T - .7\sqrt{\Omega k_z v_T})$, which is the two-stream instability. This is in agreement with previous predictions. But, for thermal energies above 20 eV, the discriminant becomes negative abruptly. Therefore, the real part of ω changes abruptly from $\Omega/2$ to $\Omega/4$. The electron gas remains unstable, since there is always at least one positive imaginary root.

Murakami and Lidsky have shown[10] the time development of the parallel-energy distribution function of one of the beams. They have also shown an oscilloscope display[11] of an electrostatic probe signal amplified by a tuned amplifier from which it can be seen that during the first microsecond the $\Omega/2$ signal is picked up by the probe. This signal disappears after 1 μs. This does not imply stabilization, since we showed that the frequency changes abruptly and, therefore, it was not recorded. As the temperature of the electron gas changes, its dielectric properties change. This may account for the change in frequency. It is also obvious that an instability still exists,[12] since each beam has a bump-on-tail distribution. In addition, the beams are not hot enough for the two-stream instability to disappear.

Thus in filamentary counterstreaming electron beams the dominating instability occurs at $\Omega/2$ frequency. After some thermalization this frequency changes, but the plasma remains unstable. This is very consistent with experimental observations.

References

1. B. J. Maxum and A. W. Trivelpiece, J. Appl. Phys. 36, 481 (1965).

2. C. Etievant and M. Perulli, in P. Hubert (Ed.), Proceedings of the Sixth International Conference on Ionization Phenomena in Gases, Paris 1963 (S. E. R. M. A., Paris, 1964).

3. M. Murakami and L. M. Lidsky, Phys. Rev. Letters 24, 297-300 (1970).

4. M. Murakami, Ph. D. Thesis, Department of Nuclear Engineering, M. I. T., November 1967.

5. E. G. Harris, J. Nucl. Energy: Pt. C 2, 138 (1961).

6. G. N. Watson, A Treatise on the Theory of Bessel Functions (The Macmillan Company, New York, 1945).

7. B. D. Fried and S. D. Conte, The Plasma Dispersion Function (Academic Press, Inc., New York, 1961).

8. A. Hershcovitch, S. M. Thesis, Department of Nuclear Engineering, M. I. T., to be submitted in December 1973.

9. M. Abramowitz and I. A. Stegun, Handbook of Mathematical Functions (Dover Publications, Inc., New York, 1965).

10. M. Murakami and L. M. Lidsky, op. cit., see Fig. 2, p. 299.

11. Ibid., see Fig. 3, p. 299.

12. Ibid., see Fig. 4, p. 299.

IV. PLASMAS AND CONTROLLED NUCLEAR FUSION

D. Fusion-Related Studies

Academic Research Staff

Prof. L. M. Lidsky
Prof. R. A. Blanken

Graduate Students

A. Pant
G. W. Braun

1. EXPERIMENTAL DETERMINATION OF THE EXPECTED LIFETIME OF A THETA-PINCH FIRST WALL

A. Pant, L. M. Lidsky

Theta Pinch: General Description

A pulsed fusion reactor (θ-pinch) is envisaged[1] as an evacuated toroidal reaction chamber in which an initially ionized deuterium-tritium mixture is heated to thermonuclear temperatures by an imploding magnetic field. Surrounding the reaction chamber is a "blanket" wherein the reaction kinetic energy of the 14-MeV neutrons is converted to thermal energy.

The fusion plasma is created in two stages of magnetic compression (Fig. IV-14). A shock magnetic field with rise time of a few nanoseconds and magnitude 1-2 T is produced in the reaction chamber by a rapidly rising current in the first wall. This shock-heats the plasma to 1-2 keV. Following this, a slower rise time (10-20 ms) field of magnitude 10-20 T is created by turning on an outer compression coil. The plasma is adiabatically heated to thermonuclear temperatures (10-15 keV). The duration of the thermonuclear burn is expected to be 50-100 ms, with a cycle time of 5-10 s (Fig. IV-15). A fresh charge of gas is introduced into the chamber and the cycle is repeated.

The vacuum wall of the reaction chamber is approximately 1 cm thick and is divided into 8-10 azimuthal sections (Fig. IV-16), which are insulated from each other. The shock magnetic field is created by applying a high-voltage pulse across each gap ("feed slot") simultaneously.

The adiabatic compression coil surrounds the shock coil and is separated from it by an inner blanket. The inner blanket provides for first-wall cooling and neutron moderation, and also reduces high-energy neutron damage to the compression coil.
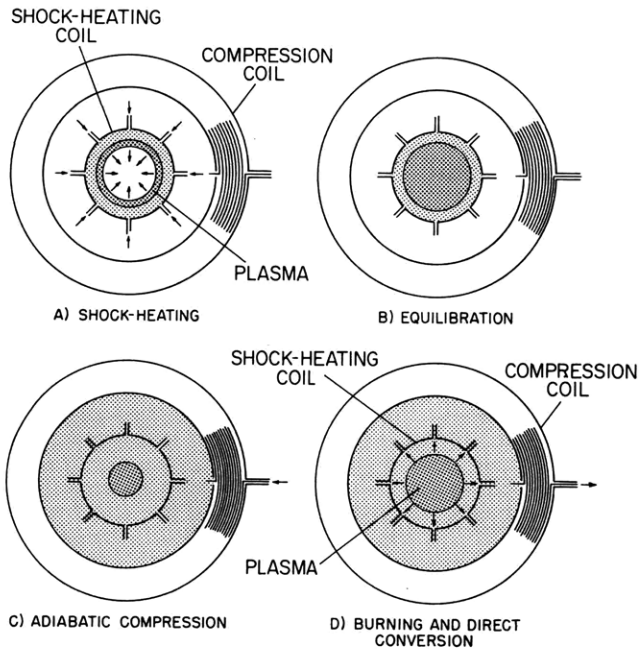
Fig. IV-14.

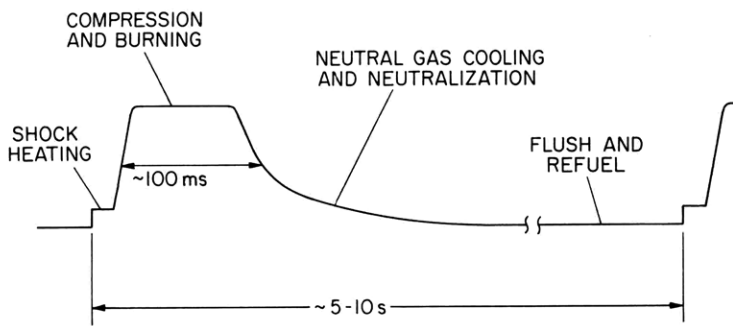Plasma heating and burning in a staged, θ-pinch, pulsed reactor. (From Burnett et al.[1])

Fig. IV-15.

Magnetic field in a pulsed, high-β, θ-pinch, reactor vs time, showing the time history of heating, burning, cooling, and refueling. (From Burnett et al.[1])
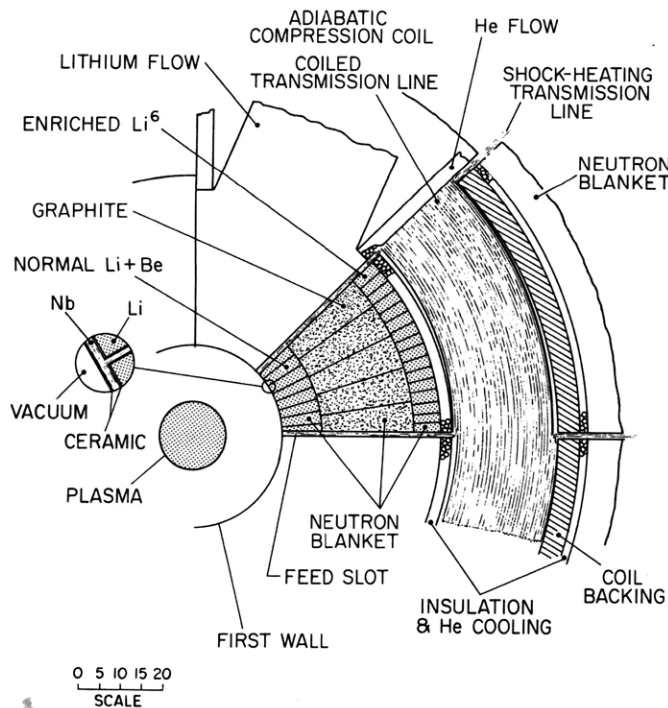
Fig. IV-16.

Core and compression coil of a pulsed, θ-pinch reactor. (From Burnett et al.[1])

Quantification of Dominant Heat Loads

Typical reactor parameters, shown in Table IV-1, are used to determine which heat loads are to be simulated, and their values.

For a given reactor thermal output, the energy flow through the first wall per pulse can be calculated simply from reactor size, load factor, and burn duration. Figure IV-17 shows typical values of energy flow per unit length for a 3 GW(th) reactor with load factor 0.02 and burn duration of 0.1 s. Curve C indicates the energy flow required for economic feasibility.[2]
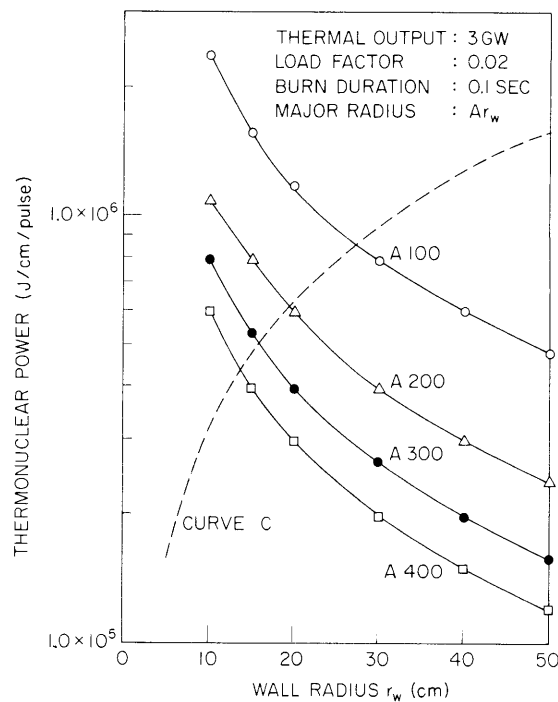

Fig. IV-17. Thermonuclear power vs wall radius.

Blanket neutronic studies[3,4] have shown that considerations of neutron economy and tritium breeding demand that the first wall be approximately 1 cm thick. They also indicate that, of the total energy release per neutron in the blanket by both primary recoil and secondary gamma-ray effects, approximately 5% is deposited uniformly throughout the first wall.

Bremsstrahlung radiation energy is a plasma temperature-dependent fraction of the thermonuclear energy, and for reactor-type plasmas (10-15 keV) this fraction is approximately 1%. The energy is absorbed in the first few millimeters of the vacuum wall.
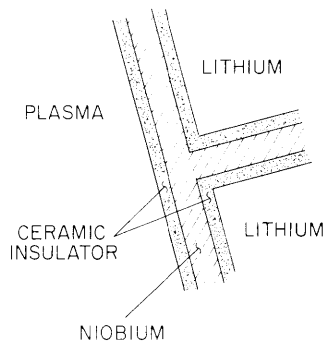
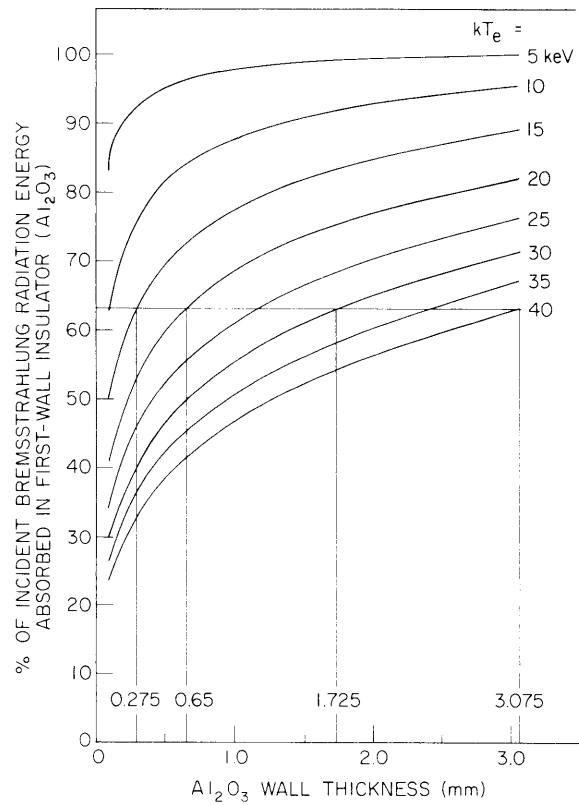Fig. IV-18.   Detail of first wall.

Fig. IV-19.   Percent of incident Bremsstrahlung radiation energy absorbed in the
first-wall insulator (Al_2O_3), plotted against the wall thickness, for
several different values of the electron temperature of the plasma
that emits the radiation.   (From Burnett et al.[1])

Plasma physics criteria governing the shock-heating of the plasma, and the fact that the first wall is cooled by liquid lithium, demand that the dual-purpose vacuum wall/shock coil be electrically insulated from the plasma and the coolant. Therefore it has been proposed[1] that the first wall be a composite structure of a suitable niobium alloy "sandwiched" between two layers of insulating material (Fig. IV-18).

The failure of the first wall is governed by the strength of the niobium alloy rather than the insulator. As 80-90% of the Bremsstrahlung energy is absorbed in the insulating material (Fig. IV-19), and is conducted through the metal, the dominant effect of the Bremsstrahlung radiation is to load the interface between the insulating material and the metal, rather than the metal itself. The major concern for this study is the integrity of the metal, and not the interface strength, although this is of general importance. Thus Bremsstrahlung loading may be neglected in comparison with neutronic heating in establishing failure criteria.

The thermonuclear energy per pulse can be expressed in terms of the final compression ratio of the plasma, x_f, and the final magnetic field, B_f (Table IV-1). The thermal load from electrical heating is a function of the shock field, B_{sh}. The ratio B_f/B_{sh} can be expressed in terms of x_f/x_{sh}, where x_{sh} is the compression ratio after the shock pulse. The quantity x_{sh} can be evaluated in terms of the dynamics of the shock phase of the pulse. Hence the electrical heating can be found in terms of the thermonuclear

Table IV-1. Typical reactor operating parameters.

OUTPUT	3 GW (th)
COIL RADIUS, r_w	25 cm
MACHINE ASPECT RATIO, A	200
NUMBER OF FEED SLOTS	10
FINAL COMPRESSION RATIO, x_f	0.2
FINAL MAGNETIC FIELD, B_f	15 T
FINAL PLASMA TEMPERATURE, T_f	15 keV
SHOCK MAGNETIC FIELD, B_{sh}	2.1 TESLA
BURN DURATION, τ_b	0.1 sec
CYCLE TIME, τ_c	5 sec
SHOCK PULSE RISE TIME, τ_r	50 nsec
FIRST-WALL AMBIENT TEMPERATURE	$600° - 1000° C$
NEUTRONIC HEAT LOAD	2.4×10^4 J/cm/pulse
BREMSSTRAHLUNG HEAT LOAD	5.0×10^3 J/cm/pulse
JOULE HEATING DUE TO SHOCK PULSE	3.2 J/cm/pulse

energy. For typical reactor operating conditions (Table IV-1) this load is three to four orders of magnitude less than the neutron load, and can be neglected.

The dominant load in the first wall is caused by neutronic and gamma backshine heating for typical reactor operating conditions. Some further reactor design considerations will be used to justify the choice of a suitable model, and determine relevant scaling laws for the experiment.

Determination of Model Parameters

Plasma heating considerations demand that the first wall of the reactor be segmented azimuthally, with each section insulated from its neighbors. Engineering considerations will probably require that the reactor be constructed in segments along the toroidal direction. Thus one section of the reactor first wall (Fig. IV-20) can be modeled without loss of generality.
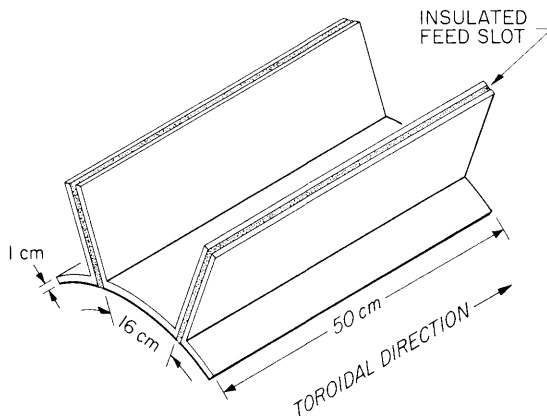

Fig. IV-20.   Dimensions and geometry of one section of the first wall.

For the thickness/radius ratios of interest here, curvature effects are negligible, and the model can be constructed in slab geometry.

The presence of insulating material between each section in the azimuthal direction will not allow for movement in this direction. In the toroidal direction, however, the reactor will probably be made of individually cooled sections that allow for expansion between them. Thus realistic boundary conditions for the model are that it be clamped in the azimuthal direction, and free in the toroidal direction.

Model prototype scaling laws can now be established by deducing dimensionless relationships (Fig. IV-21) between expected stress levels, operating conditions, and material properties.

The temperature and stress oscillations in a slab subjected to cyclic thermal loading are shown in Figs. IV-22 and IV-23. For reactor operating conditions, the maximum temperature oscillation is expected to be approximately 80-160° F and the maximum

FUNCTIONAL DEPENDENCE OF TEMPERATURE

$$\frac{T(x/L, t/\tau_c)}{T_o} = f\left\{\frac{\lambda}{L}, \frac{t}{\tau_c}, F_o, Bi\right\}$$

FUNCTIONAL DEPENDENCE OF STRESS

$$\frac{\sigma(x/L, t/\tau_c)}{\alpha E T_o} = f\left\{\frac{\lambda}{L}, \frac{t}{\tau_c}, F_o, Bi\right\} \qquad 1$$

THERMAL LOAD COEFFICIENT

$$T_o = \frac{q''' L^2}{k} \qquad 2$$

BIOT NUMBER:

$$Bi = \frac{hL}{k}$$

FOURIER MODULUS
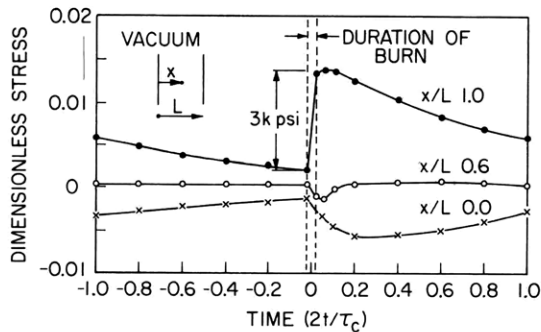
$$F_o = \frac{\alpha \tau_c}{2L^2} \qquad 3$$

WHERE

λ: ANY SCALE LENGTH
t: ANY RELEVANT TIME
h: HEAT TRANSFER COEFFICIENT AT WALL/LITHIUM INTERFACE
k: THERMAL CONDUCTIVITY OF METAL
α: THERMAL DIFFUSIVITY OF METAL
q''': VOLUMETRIC HEAT LOAD
L: FIRST-WALL THICKNESS
τ_c: CYCLE TIME
α: THERMAL COEFFICIENT OF EXPANSION
E: YOUNG'S MODULUS
x: DISTANCE INTO WALL FROM VACUUM

Fig. IV-21.

Dimensional dependence of stress profiles.

LOAD FACTOR $\tau_b/\tau_c = 0.02$
BOIT # : 15.625
FOURIER # : 0.4499

Fig. IV-22.

Temperature oscillations in a slab of thickness L.

LOAD FACTOR $\tau_b/\tau_c = 0.02$
BIOT # : 15.625
FOURIER # : 0.4499

Fig. IV-23.

Stress profiles.

MODEL HEAT LOAD:

$$(H)_{MODEL} = \frac{(H)_{PROTOTYPE}}{n_1^2 n_2} \qquad 4$$

MODEL SCALE TIME:

$$(t)_{MODEL} = \frac{(t)_{PROTOTYPE}}{n_1^2} \qquad 5$$

n_1: SCALE FACTOR FOR WIDTH AND THICKNESS
n_2: SCALE FACTOR FOR LENGTH
FOR $n_1 = 4$; $n_2 = 8$

$(H)_{PROTOTYPE}$	$(H)_{MODEL}$	$(\tau_b)_{PROTOTYPE}$	$(\tau_b)_{MODEL}$	$(\tau_c)_{PROTOTYPE}$	$(\tau_c)_{MODEL}$
0.2 mJ/pulse	1.6 kJ/pulse	0.1 sec	6 msec	5 sec	0.3 sec

Fig. IV-24.

Heat loads and time values for the model.

stress oscillation about 3-6 kpsi in typical niobium alloys.[5] Yield strengths for such alloys are 30-40 kpsi, and hence failure is expected to be dominated by high cycle fatigue.[6] In order to simulate the stress levels, model and prototype must have the same values for the Fourier modulus, F_o, and the thermal load coefficient, T_o. To establish failure criteria, model and prototype must be constructed of the same material, and be operated at the same ambient temperature. Thus, relationships among heat load, heating pulse duration, cycle time, and geometric scale factor are immediately established.

Stress-strain relationships and failure levels become grain orientation-dependent if more than 5% of the grains are on the surface of the model.[7] The governing dimension is model thickness, and randomness of grain orientation can be retained in niobium alloys of interest (50 μm grain size)[5] by keeping model thickness above 0.2 cm, which corresponds to a maximum thickness scale factor of 5. The scale factor, n, is chosen as 4 for model width and thickness, and 8 for length.

For the given reactor parameters, the pulse duration in the model, $(\tau_b)_{mod}$, will be 6 ms, with a cycle time, $(\tau_c)_{mod}$, of 300 ms (Fig. IV-24). The heat load in the model is 0.96 kJ/pulse corresponding to the reactor of Table IV-1 (1.6 kJ/pulse is equivalent

Table IV-2. Possible options for varying loading conditions.

OPTION	EFFECT
REDUCE CYCLE TIME, τ_c	LOAD FACTOR INCREASED, HIGHER REPETITION RATE
INCREASE HEAT LOAD PER PULSE	LOAD FACTOR UNALTERED. HIGHER TEMPERATURE PEAKS AND CYCLIC STRESSES MAXIMUM LOAD IS 50-60% HIGHER THAN WALL FLUX LIMIT FOR LOAD FACTOR 0.02
REDUCE MODEL SIZE	TEST FOR EXTREME LOADING CONDITIONS SIZE OF MODEL CAN BE CORRELATED WITH VALID REACTOR SIZE

to a time-averaged power throughout of 1 kW/cm^2). This determines the required power levels to be produced in the laboratory. It is intended to provide for a maximum model loading of 2.5 kJ/pulse with controllable cycle times. Thus the model can be tested for loading conditions 50% greater than required for economic feasibility. Table IV-2 shows the possible options. Models can be tested over a wide range of loads, and baseline lifetimes can be evaluated.

Design of Experiment: Present Status

The model must be tested at different operating temperatures. Initial, low-temperature tests will enable us to determine stress levels by using strain-gauge techniques,

while high-temperature tests will be used to establish failure criteria. A controlled temperature environment will be used for the tests, and will provide for uniform ambient temperature. Simulation of first-wall cooling will be achieved by free convection cooling with a nonconducting eutectic salt (FLIBE).

The model (Fig. IV-25) forms part of the secondary circuit of a pulse transformer, whose primary is triggered with a high-voltage, high-current SCR. The time between pulses can be varied to suit required loading conditions. The 60-Hz ac line, when combined with judicious use of pulse transformer properties, will be used to provide a heating pulse of the required duration.
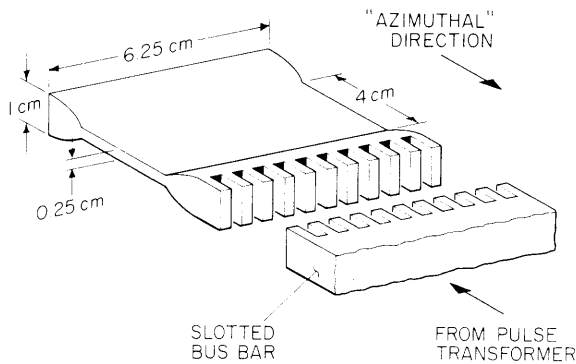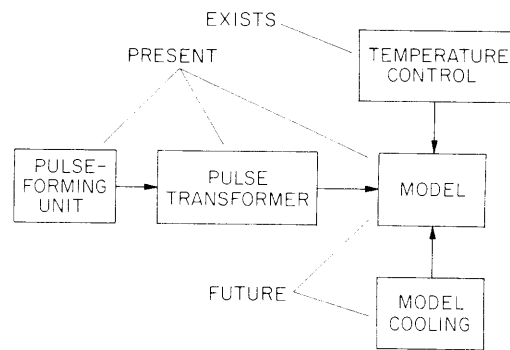

Fig. IV-25. Model details.

Fig. IV-26. Components of apparatus, and status of the experiment.

The shaped ends of the model serve the dual purpose of minimizing end losses and providing the required boundary condition in the azimuthal direction. The thermal response time of the ends will be much larger than that of the model strip; hence, for cyclic loading the model can be considered to have fixed ends. The boundary condition in the toroidal direction will be neither fixed nor free; probably closer to reality than a pure "free" boundary would be. As we have mentioned, failure is expected to be dominated by high cycle fatigue. The imposed boundary conditions imply that a combination of two failure modes may be present. In the azimuthal direction, cyclic compressive stresses, and hence buckling failure, will dominate. Model lifetime will depend on both heat-load magnitude and model width. In the toroidal direction, the stresses are tensile cyclic, and hence surface cracking is expected.

The present phase of this study (Fig. IV-26) involves the construction of the experiment, in particular, the pulse transformer and electrical heating unit. The detailed design and manufacture of model assemblies, complete with provision for cooling, will be in the next phase, after which tests of stress level and failure can be started.

References

1. S. L. Burnett et al., "A Reference Theta Pinch Reactor (RTPR)," Los Alamos Report LA-5121-MS, December 1972.

2. G. W. Braun, "Design of a Natural Uranium/Lithium Blanket for a Breakeven Theta Pinch," Nuclear Engineering Thesis and S. M. Thesis, Department of Nuclear Engineering, M. I. T., June 1, 1973.

3. D. Steiner, "The Nuclear Performance of Fusion Reactor Blankets," Nuclear Fusion Reactor Conference, Culham Laboratory, Abington, Berkshire, England, September 17-19, 1969.

4. A. J. Impink, Jr., "Neutron Economy in Fusion Reactor Blanket Assemblies," Technical Report 434, Research Laboratory of Electronics, M. I. T., June 22, 1965.

5. Product Data, Wah Chang Albany Company, Albany, Oregon; n. d.

6. L. F. Coffin and R. M. Goldhoff, "Predictive Testing in Elevated Temperature Fatigue and Creep: Status and Problems," American Society for Testing Materials, Report STP 515, 1972, pp. 22-74.

7. F. A. McClintock and A. Argon, Mechanical Behavior of Materials (Addison-Wesley Publishing Co., South Reading, Mass., 1966).

IV. PLASMAS AND CONTROLLED NUCLEAR FUSION

F. High-Temperature Plasma Physics

Academic and Research Staff

Prof. B. Coppi
Dr. D. B. Montgomery*
Prof. G. Bekefi
Prof. A. Bers
Prof. R. A. Blanken
Prof. L. M. Lidsky

Prof. P. A. Politzer
Prof. R. J. Taylor
Dr. E. G. Apgar
Dr. U. Ascoli-Bartoli
Dr. P. Brossier

Dr. L. T. Ornstein
Dr. R. R. Parker
Dr. R. Pozzoli
Dr. T. J. Schep
Dr. H. N. Van der Ven
Dr. R. Van Heijningen

Graduate Students

W. A. Baan
E. L. Bernstein
D. L. Cook
R. J. Hawryluk
D. P. Hutchinson

D. S. Komm
Y. Y. Lau
T. Orzechowski
G. Rewoldt

M. Simonutti
M. S. Tekula
B. V. Waddell
D. C. Watson
S. M. Wolfe

1. CURRENT-DRIVEN INSTABILITIES IN A PLASMA

M. S. Tekula, A. Bers

It was reported by Bobrovskii et al.[1] that when the Tokamak TM-3 device was operated in a region of high electron temperature and low plasma density ($T_e > 500$ eV and $n < 6 \times 10^{12}$/cm^3) that ions were observed whose energy could not be explained by coulomb energy transfer from the electrons to the ions. This was a regime of operation where the plasma was collisionless and had an anomalously high resistance. Attempts have been made to explain these effects on the basis of collective interactions.[2] Lack of knowledge of the precise turbulent spectra has prevented reaching a definite conclusion about the validity of this explanation.

We now report the results of detailed calculations on the spectra of electrostatic waves in a homogeneous, fully ionized, collisionless plasma in a magnetic field. The ion distribution function is assumed Maxwellian and the electron distribution function is taken to be Maxwellian with a drift velocity relative to the ions. The parameters that we picked correspond to two experiments reported by Bobrovskii et al.,[1] and are listed in Table IV-3. In the first experiment, the current was held fixed at 12 kA and the magnetic field was varied from 10 kG to 26 kG. In the first case 3% of the ions were heated. Fewer and fewer were observed to be heated as the magnetic field was increased, until none were observed at 26 kG. In Table IV-3, in TM-3 (a) the current was 12 kA, and

---

*Dr. D. Bruce Montgomery is at the Francis Bitter National Magnet Laboratory.

Table IV-3. Parameters for TM-3 experiments.

	(a)	(b)	(c)	(d)
ω_{ci}	9.6×10^7/s	2.5×10^8/s	2.5×10^8/s	2.5×10^8/s
ω_{pi}/ω_{ci}	13.8	5.3	5.3	5.3
T_e/T_i	20	20	80	180
U/v_i	38	38	76	114
U/v_e	0.1	0.1	0.2	0.2
q	7	17.5	9	6
λ_{Di}	5.3×10^{-3} cm	5.3×10^{-3} cm	5.3×10^{-3} cm	5.3×10^{-3} cm
a_i	7×10^{-2} cm	2.8×10^{-2} cm	2.8×10^{-2} cm	2.8×10^{-2} cm
λ_{De}	2.4×10^{-2} cm	2.4×10^{-2} cm	4.7×10^{-2} cm	7.1×10^{-2} cm
a_e	7×10^{-3} cm	3×10^{-3} cm	6×10^{-3} cm	9×10^{-3} cm
ν_{ii}	9×10^3/s	9×10^3/s	9×10^3/s	9×10^3/s
ν_{ei}	1.4×10^3/s	1.4×10^3/s	0.19×10^3/s	0.056×10^3/s
ν_{ei}^ϵ	1.52/s	1.52/s	0.2/s	0.06/s

(a) $I_{oe} = 12$ kA, $B_o = 10$ kG, $T_e = 1$ keV
(b) $I_{oe} = 12$ kA, $B_o = 26$ kG, $T_e = 1$ keV
(c) $I_{oe} = 24$ kA, $B_o = 26$ kG, $T_e = 4$ keV
(d) $I_{oe} = 36$ kA, $B_o = 26$ kG, $T_e = 9$ keV

NOTE: These parameters are common to all cases considered here:
$a = 8$ cm, $R = 40$ cm, $T_i = 50$ eV, $m_i/m_e = 1836$, $n = 10^{18}$/m^3.

the magnetic field 10 kG; in TM-3 (b) the magnetic field was 26 kG. In the second exper-
iment the magnetic field was fixed at 26 kG and the current was varied from 7 kA to
36 kA. In TM-3 (c) the current was 24 kA; in TM-3 (d) the current was 36 kA. It was
observed that the number of ions heated was 5% and 13%, respectively. For all cases
we took the density to be $1 \times 10^{12}/cm^3$. The ratio of electron drift velocity to ion sound
speed $(u_{\parallel e}/c_s)$ was observed to be 12 for all cases.

The dispersion relation can be written

$$1 + T + K^2 A/2 + (T^3/M)^{1/2} (\Omega - K_\parallel U)/K_\parallel \sum_n Z(\zeta_{ne}) \Gamma_n(\lambda_e) + (\Omega/K_\parallel) \sum_n Z(\zeta_{ni}) \Gamma_n(\lambda_i) = 0,$$

(1)

where $\Omega = \omega/\omega_{ci}$, $K = k v_i/\omega_{ci}$, $T = T_i/T_e$, $M = m_i/m_e$, $\Lambda = \omega_{ci}^2/\omega_{pi}^2$, $U = u_{\parallel e}/v_i$,
$v_i = (2\kappa T_i/m_i)^{1/2}$, $\lambda_{e,i} = (k_\perp a_{e,i})^2$, $a_{e,i} = v_{e,i}/\omega_{ce,i} \sqrt{2}$, $\zeta_{ni} = (\Omega - n)/K_\parallel$, $\zeta_{ne} =$
$(\Omega - nM - K_\parallel U)/(K_\parallel (M/T)^{1/2})$, $\Gamma_n(\lambda) = I_n(\lambda) e^{-\lambda}$. The modified Bessel function is $I_n(\lambda)$, and
Z is Fried and Conte's plasma dispersion function.[3] Figures IV-27 through IV-29 rep-
resent an exact computer solution of the dispersion relation in Eq. 1 for the parameters
listed in Table IV-3.

Before discussing the results, we shall consider the conditions under which the
homogeneous and collisionless plasma assumptions may be applicable to the Tokamak
experiments under consideration. The coulomb collision times, summarized in
Table IV-3, are found to be negligible compared with the growth rates. The longest
wavelength in the radial direction that we have considered is ~0.8 cm, which is much
smaller than the 8-cm plasma radius. In any case, the density in a Tokamak is rela-
tively homogeneous across the plasma cross section except at the periphery. The effects
of the magnetic field inhomogeneity should be explored by using a dispersion relation
based on the actual zero-order particle orbits in the Tokamak. We shall argue, however,
that for the short-wavelength, fast-growing modes which we found, this is not necessary.
In a Tokamak, particles are assumed to be in the banana regime when their effective col-
lision frequency ν_{eff} is much smaller than the bounce frequency ω_b. For the ions $\nu_{eff} =$
$\nu_{ii}/(r/R)$, which for a typical ion located at half the plasma radius $r = a/2$ is $10^5/s$; for
the TM-3 experiments we found $\omega_B^i \sim 10^3$-$10^4/s$. For the electrons, $\nu_{eff} = \nu_{ei}(r/R) \sim 10^3$,
but $\omega_B^e \sim 10^6$, for $r = a/2$. Electrons start to be trapped when $v_\parallel/v_\perp < (2r/R)^{1/2}$, evalu-
ated at the minima of the magnetic field. For $r = a/2$ this means that we have to take
particle trapping into account for angles of propagation with respect to the magnetic field
greater than about 70°. We find, however, that the most unstable ion-acoustic and mag-
netoacoustic waves lie outside the region of particle trapping. For $r = a/2$, 30% of the
electrons are trapped. Since the typical oscillation frequency is $\omega_r \sim 7.5 \times 10^8/s$, and
the growth rate is $7.5 \times 10^7/s$, while the bounce frequency is $\omega_B^e \sim 10^6$, we can say that

on the time scale of the unstable waves the current that drives the instabilities is the same as that used in the case of no trapping; hence the growth rates are not modified by the trapped particles. In the case of the ion cyclotron waves we have to examine Landau damping in toroidal coordinates, because this wave lies in the trapped particle regime. But, since the average velocity of trapped electrons is $\langle v_{\|T} \rangle \sim 10\, c_s$ while the parallel phase velocity of the wave is $c_s \cos\theta$, we could not get any trapped particle-wave resonance. Hence, for all the unstable waves we are considering, the homogeneity assumption is a good one.

Now we turn our attention to the spectra. Figures IV-27 through IV-29 show the results of computations based on the complete dispersion relation (Eq. 1). The solid lines are contours of constant normalized real frequency Ω_R; dashed lines are contours of constant normalized imaginary frequency Ω_I.

We shall discuss some approximate solutions to Eq. 1, and see how they can be applied to explain the computed results shown in the figures. To solve Eq. 1, we assume that the waves are weakly damped or growing ($\Omega_I/\Omega_R \ll 1$), where $\Omega = \Omega_R + j\Omega_I$.

Consider, first, the slow magnetoacoustic wave $\Omega_R \ll 1$. The dispersion relation for this wave can be derived by dropping all but the $n = 0$ term in Eq. 1. Then, assuming $|\zeta_{oe}| \ll 1$ and $|\zeta_{oi}| \gg 1$ (which implies $T_e/T_i \gg 1$), and $\Gamma_0(\lambda_i) \approx 1$, $\Gamma_0(\lambda_e) \approx 1$ (that is, $K_\perp^2 \ll 1$), and dropping terms of order ζ_{oe}^2 and ζ_{oi}^{-6} in the Z-function expansions, we get

$$\Omega_R/K_\| \cong 1/(2T)^{1/2}; \quad (\omega/k_\| \cong c_s) \tag{2}$$

$$\Omega_I \cong (\pi/8M)^{1/2} K_\| \{U-[1/(2T)^{1/2}](1 + (M/T^3)^{1/2} e^{-1/(2T)})\}.$$

Equation 2 implies that both the real and imaginary parts of the frequency should be vertical lines on a $(K_\perp, K_\|)$ plot (see Fig. IV-27). The imaginary part deviates from vertical because, for a fixed ω, as $k_\perp$ becomes large compared with $k_\|$, the wave goes through a resonance ($\omega = \omega_{ci} \cos\theta$) and is strongly Landau-damped. This is indicated in Fig. IV-27 by the curvature of the contours of the constant imaginary part. The value of $K_\|$ at which this occurs is $K_\| \approx 0.5(2T)^{1/2}$, that is, $k_\|\lambda_{Di} \sim (T_i/T_e)^{1/2} \omega_{pi}/2\omega_{ci}$. This is in agreement with Fig. IV-27. Notice that the magnetic field is not an important parameter in determining the extent of the normalized turbulent spectrum (compare Fig. IV-27a and 27b). On the other hand, the effect of changing the current and temperature ratio is more significant, as Eq. 5 implies (see Fig. IV-27b, 27c, 27d).

Next we shall consider the ion acoustic wave. The conditions under which this can be derived from Eq. 1 are $\Omega_R \gg 1$, $|\zeta_{oe}| \ll 1$, $|\zeta_{ne}| \gg 1$, $|\zeta_{ni}| \gg 1$, $\lambda_{e,i} \ll 1$. With these assumptions and dropping terms of order ζ_{oe}^2, ζ_{oi}^{-6}, ζ_{ni}^{-4}, ζ_{ne}^{-4}, we get

$$\Omega_R / K \cong 1/(2T)^{1/2}; \quad (\omega/k = c_s)$$

$$\Omega_I \cong (\pi/8M)^{1/2} K\{U - [1/((2T)^{1/2} \cos\theta)] [1 + (M/T^3)^{1/2} \exp(-1/2T \cos^2\theta)]\}$$

(3)

when $K^2 \ll 2T/A$ (that is, $k^2 \lambda_{Di}^2 \ll (T_i/T_e)$), and

$$\Omega_R \cong 1/A^{1/2}; \quad (\omega \approx \omega_{pi})$$

$$\Omega_I = (\pi T^3/M)^{1/2} [1/[K^2 A^{3/2}]] \left\{ U - \left(1/\left(A^{1/2}K_\parallel\right)\right) \left[1 + (M/T^3)^{1/2} \exp(-1/AK_\parallel^2)\right]\right\}$$

(4)

when $K^2 \gg 2T/A$ (that is, $k^2 \lambda_{Di}^2 \gg (T_i/T_e)$). The normalized velocity necessary to induce unstable ion acoustic waves parallel to the magnetic field is given by

$$U > [1/(2T)^{1/2}]\{1 + (M/T^3)^{1/2} e^{-1/2T}\}.$$

(5)

This is the same velocity that is needed for magnetoacoustic waves. Hence for a magnetoacoustic wave, once the wave parallel to the field is unstable, it is unstable at all angles (cf. Eq. 2). On the other hand, the velocity necessary to induce unstable
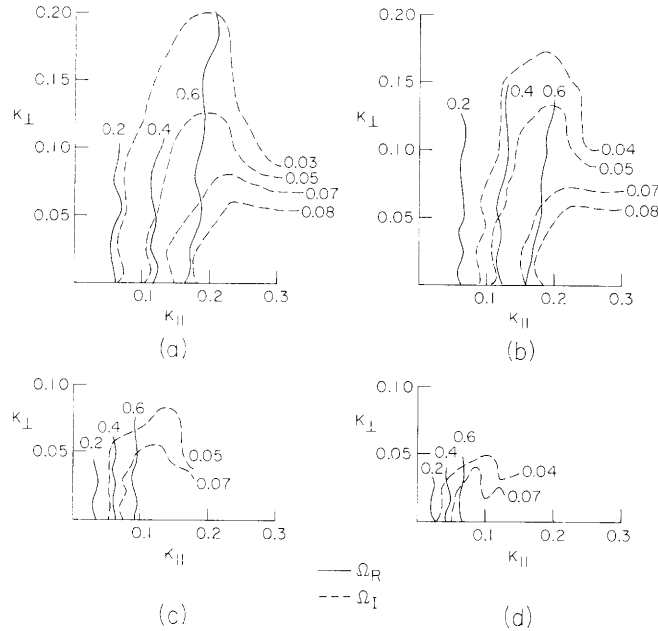

Fig. IV-27. Unstable spectra for slow magnetoacoustic waves. Contours of constant Ω_R and Ω_I.

ion acoustic waves at an angle goes up. Hence, for a fixed U, the most unstable ion acoustic wave is that parallel to the magnetic field (cf. Eq. 3 and Fig. IV-28). The maximum growth rate of the parallel ion acoustic wave will occur at $K_{\parallel} \approx 0.5(2T/A)^{1/2}$.
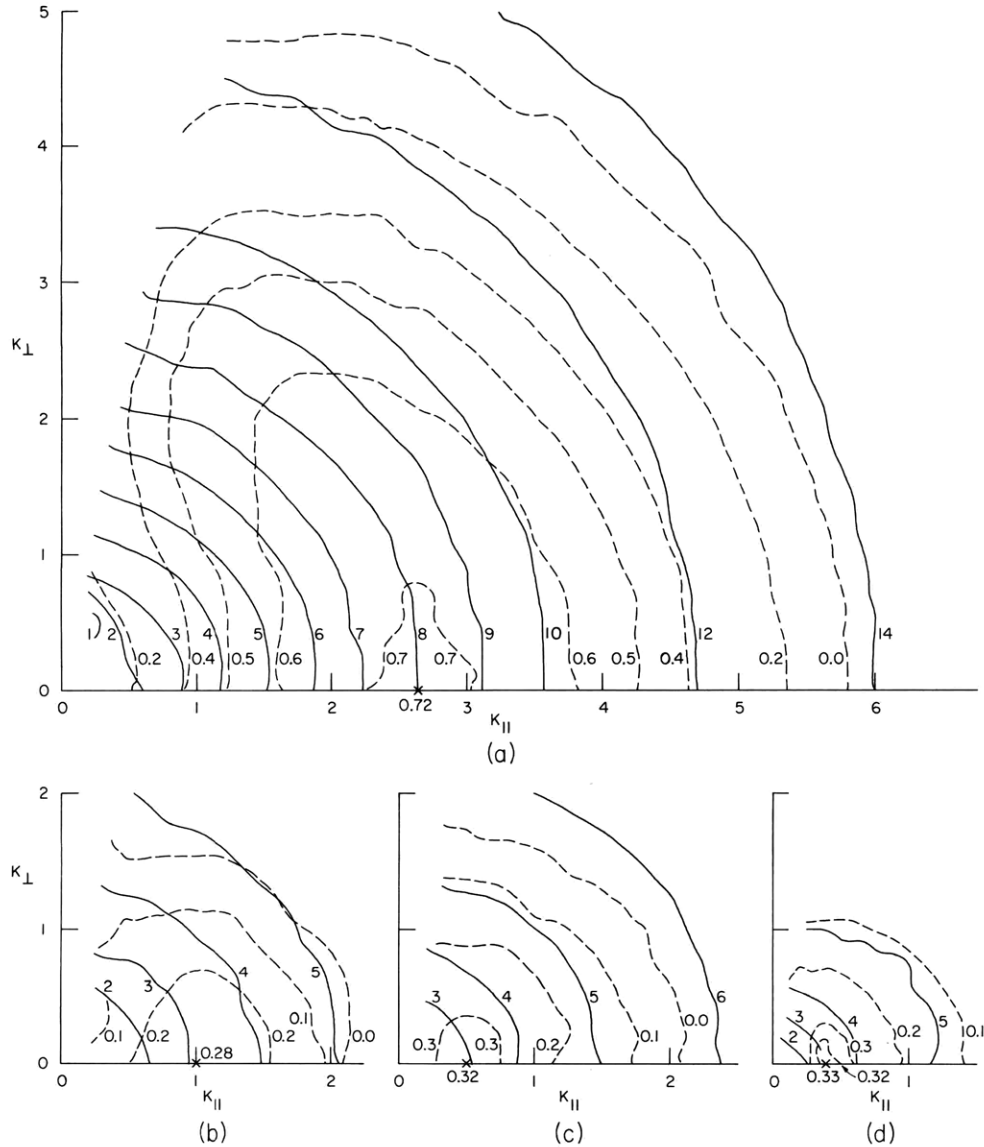

Fig. IV-28. Unstable ion acoustic spectra. Contours of constant Ω_R and Ω_I.

The extent of the unstable ion acoustic spectrum parallel to the magnetic field can be found by solving Eq. 4 with $\Omega_I = 0$. The $K_{\parallel}$ for which this occurs is given by

$$K_{\parallel}^{max} = 1 \left/ \left[A \ln \left((M/T^3)^{1/2} U^{-1} \right) \right]^{1/2} \right. .$$

(6)

From this we see that the extent of the turbulent spectrum depends strongly on the mag-
netic field and only weakly on temperature and drift velocity. In Fig. IV-28a and 28b
where the current was kept constant, we note that lowering the magnetic field broadens
the unstable spectrum (normalized) and increases the maximum growth rate. On the
other hand, comparing Fig. IV-28b, 28c, and 28d where the current is increased while
the magnetic field is kept constant, we see that the unstable spectrum (normalized) also
has an increasing maximum growth rate, but becomes narrower in k space.

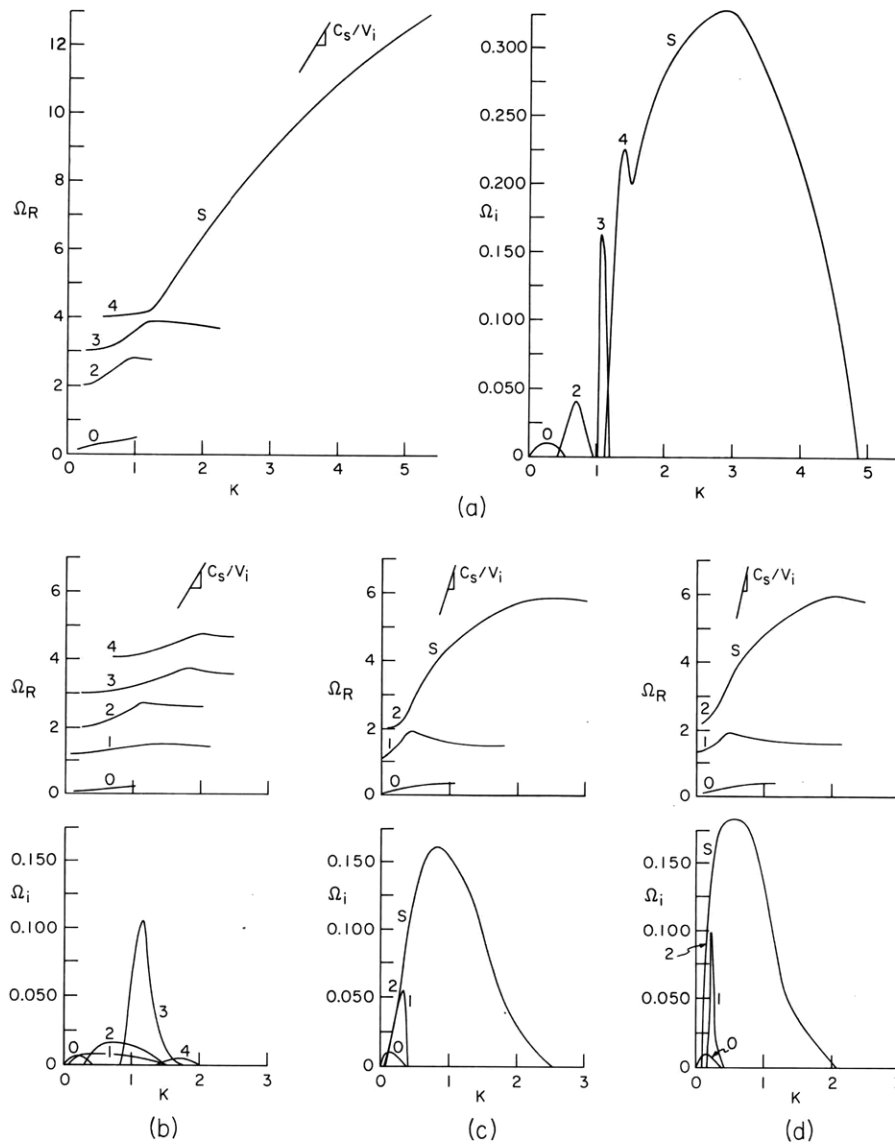The spectra in Fig. IV-28 are not complete for $\theta > 80°$ because approximately beyond

Fig. IV-29.   Unstable ion-cyclotron harmonic spectra.   Contours of con-
stant Ω_R and Ω_I when $\theta = 80°$.

this angle cyclotron harmonic waves begin to occur, and it is impractical to plot them on $(K_\perp, K_\parallel)$ diagrams.

We shall now discuss cyclotron harmonic waves. These can be derived from Eq. 1 by making the same assumptions as in the ion-acoustic case, except that now we assume $\Omega_R \sim N$, where N is the Nth cyclotron harmonic. In that case we obtain

$$\Omega_R \approx N \left\{ 1 + [T^{-1}/N!] \, (K_\perp^2/4)^N \right\}$$

$$\Omega_I \approx (\pi/MT)^{1/2} \left(K_\perp^2/4\right)^N [1/(N-1)!] \left\{ U - [N/K_\parallel] \left[1 + (M/T^3)^{1/2} \left(K_\perp^2/4\right)^N 1/N! \right] \right\}$$

(7)

The solution in Eq. 7 is restricted to rather low harmonic numbers because otherwise $K_\perp$ exceeds unity. Also, it can be seen from Fig. IV-29 that at steep angles to B_o a mixture of ion-cyclotron harmonic waves, as well as ion acoustic waves, is frequently encountered. The transition between these two types of wave has a complicated dependence upon plasma parameters, and is not yet fully understood.

The velocity needed to induce unstable cyclotron harmonic waves has been given by Kindel and Kennel.[4] They found that the ion cyclotron harmonic waves have a lower threshold than the ion acoustic waves when $0.1 < T_e/T_i < 8$. Hence in the Tokamak TM-3 the parallel ion acoustic waves have the lowest threshold.

In conclusion, we have established the detailed spectra for unstable waves in a homogeneous plasma with parameters corresponding to experiments in the Tokamak TM-3. From these we find that keeping I_{oe} constant and lowering B_o broadens and heightens the growing spectrum. We may therefore expect that the observed heating of a small percentage of the ions may be explained by quasilinear diffusion into the tail of the distribution function. On the other hand, for experiments in which B_o is kept fixed and I_{oe} is increased, the narrowing and heightening of the unstable spectrum would favor a model of ion heating by trapping. These conclusions must, of course, be substantiated by detailed nonlinear model calculations.

References

1. G. A. Bobrovskii, E. I. Kuznetsov, and K. A. Razumova, Zh. Eksp. Teor. Fiz. [Sov. Phys. – JETP] 59, 1103 (1970).

2. A. Bers, B. Coppi, T. Dupree, R. Kulsrud, and F. Santini, "Turbulence in Confined Plasmas at High Electric Fields," in Plasma Physics and Controlled Nuclear Fusion Research, 1971, Vol. II (International Atomic Energy Agency, Vienna, 1971), pp. 247-263.

3. B. D. Fried and S. D. Conte, The Plasma Dispersion Function (Academic Press, Inc., New York, 1961).

4. J. M. Kindel and C. F. Kennel, J. Geophys. Res. 76, 3055 (1971).